# Analysis of Gaussian beam and Bessel beam driven laser accelerators

B. Hafizi,[1,*] A. K. Ganguly,[1] A. Ting,[2] C. I. Moore,[1,†] and P. Sprangle[2]
[1]*Omega-P, Inc., P.O. Box 202008, New Haven, Connecticut 06520-2008*
[2]*Plasma Physics Division, Naval Research Laboratory, Washington, D.C. 20375-5346*
(Received 27 April 1999)

This paper presents a comparison of Gaussian and Bessel beam driven laser accelerators. The emphasis is on the vacuum beat wave accelerator (VBWA), employing two laser beams of differing wavelengths to impart a net acceleration to particles. Generation of Bessel beams by means of circular slits, holographic optical elements, and axicons is outlined and the image space fields are determined by making use of Huygens' principle. Bessel beams—like Gaussian beams—experience a Guoy phase shift in the vicinity of a focal region, resulting in a phase velocity that exceeds *c*, the speed of light *in vacuo*. In the VBWA, by appropriate choice of parameters, the Guoy phases of the laser beams cancel out and the beat wave phase velocity equals *c*. The particle energy gain and beam quality are determined by making use of an analytical model as well as simulations. The analytical model—including the $\mathbf{v}\times\mathbf{B}$ interaction—predicts that for equal laser powers Gaussian and Bessel beams lead to identical energy gains. However, three-dimensional, finite-emittance simulations, allowing for detuning, transverse displacements, and including all the electromagnetic field components, show that the energy gain of a Gaussian beam driven VBWA exceeds that of a Bessel beam driven VBWA by a factor of 2–3. The particle beam emerging from the interaction is azimuthally symmetric and collimated, with a relatively small angular divergence. A table summarizing the ratios of final energies, acceleration lengths, and gradients for a number of acceleration mechanisms is given.
[S1063-651X(99)02510-6]

PACS number(s): 41.75.Lx, 42.62.−b

## I. INTRODUCTION

Attainment of the high intensities necessary for laser-driven accelerators [1–21] requires that the beam be focused down to a waist that is a few wavelengths in diameter. For a highly focused beam, the distance over which this high intensity can be sustained is relatively short due to transverse spreading. The free-space scale length for diffraction of a collimated Gaussian beam, depicted in Fig. 1, is the Rayleigh range [22]:

$$Z_R=\pi w_0^2/\lambda, \tag{1}$$

where $w_0$ is the waist (i.e., minimum spot size) of the beam, $\vartheta=\tan^{-1}(\lambda/\pi w_0)$ is the asymptotic divergence angle, and $\lambda$ is the wavelength. The intensity may be increased by focusing the beam down to a smaller waist. This, however, reduces the Rayleigh range and hence the beam remains nearly collimated over a shorter distance in the Fresnel region (near field), while in the Fraunhofer region (far field) the beam diverges with a larger angle. Thus the interaction length may be reduced if a laser beam with a smaller waist is employed.

This trade-off between intensity and interaction length can be illustrated by an example. For a circularly polarized Gaussian laser beam, the amplitude $\varepsilon_0$ of the transverse component of the electric field is expressible as

$$|e|\varepsilon_0/(mc\omega)=4.8(\lambda/w_0)P^{1/2}(\mathrm{TW}), \tag{2}$$

where $e$ and $m$ are the electronic charge and mass, $\omega=2\pi c/\lambda$ is the frequency, $c$ is the speed of light *in vacuo*, and $P$ is the power, expressed in terawatts. The electromagnetic field associated with a laser beam is predominantly transverse. There is, in addition, a smaller longitudinal field component. The longitudinal field may be estimated from the Coulomb gauge condition $\mathrm{div}\,\mathbf{E}=0$, or $\partial E_z/\partial z=-\nabla_\perp\cdot\mathbf{E}_\perp$, where the subscripts $z$ and $\perp$ denote the longitudinal and transverse components, respectively. In order of magnitude, the amplitude $\varepsilon_z$ of the axial component of the field is given by

$$\varepsilon_z=O(\varepsilon_0/(kw_0)). \tag{3}$$

Making use of Eqs. (1)–(3), $W\equiv\varepsilon_z Z_R$—which is an estimate for the change in particle energy—is a function of the laser power only. In other words, for a given power, $W$ is the same independently of whether the laser beam is focused down to

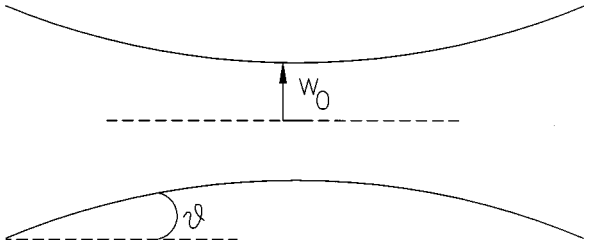


FIG. 1. Free-space diffraction of Gaussian beam. Waist (minimum spot size) is denoted by $w_0$ and $\vartheta$ is asymptotic beam divergence angle.

*Permanent address: Icarus Research, Inc., P.O. Box 30780, Bethesda, MD 20824-0780.

†Present address: Plasma Physics Division, Naval Research Laboratory, Washington, D.C. 20375-5346.

 

high intensity (and short interaction length) or only slightly focused (with a long interaction length).

It is natural to ask what the scaling of $W$ is for other mode profiles or acceleration mechanisms and if, for comparable situations, $W$ can be increased. A Gaussian beam, focused by means of spherical optical elements, is the most common form of radiation from a laser cavity [22]. A Bessel beam [23–35] is more exotic and can be generated by a circular slit, a holographic optical element, or an axicon. A Bessel beam forms a ''line'' image and thus might appear to have advantages as regards the interaction distance.

There are two insidious effects associated with diffraction. First, there is a fall-off in *intensity* with distance. The second manifestation of diffraction is more subtle. On passing through a focal region, a laser beam accumulates an axial *phase* shift. The extra phase—called the Guoy phase—effectively increases the phase velocity beyond $c$, the vacuum speed of light, and detunes the wave-particle interaction. In Ref. [35], Gaussian and Bessel beams were compared for a number of high-gradient acceleration mechanisms, assuming that the wave-particle synchronism could be maintained by some means. For example, it was shown that for a vacuum beat wave accelerator (VBWA)—wherein net acceleration is imparted by the beat wave of two laser beams of differing wavelengths—the energy gain of the two beam profiles is comparable.

The purpose of this paper is to analyze the VBWA [11,13] process in detail, supplementing the analytical work in Ref. [35] with full-scale particle simulations, and comparing the energy gain and particle beam quality for Gaussian and Bessel beams. The scalar wave equation is discussed in Secs. II and III and used to obtain expressions for the image space fields for Gaussian and Bessel beams. Experimental configurations for forming Bessel beams, such as axicons and zone plates (holograms), are outlined in Sec. IV. Expressions for the amplitudes and phase shifts are derived. The inventive step in the VBWA is that the Guoy phase of the two laser beams cancels out by proper choice of parameters, leading to a beat wave with a phase velocity equal to $c$, allowing near-synchronism with particles. Assuming a synchronous interaction, in Sec. V an analytical expression for the energy gain is derived for the Bessel beam driven VBWA using a compound axicon and compared with the corresponding expression using a Gaussian beam. The model—neglecting transverse displacements of particles and including the $\mathbf{v}\times\mathbf{B}$ interaction—predicts equal energy gains for the two configurations. Section VI presents the results of full-scale simulation studies, employing prescribed laser fields and finite-emittance particle beams, to compare the energy gain in the two cases. The simulations show that in practice the energy gain for the Bessel beam driven vacuum beat wave accelerator is a factor 2–3 less than that for a Gaussian beam driven configuration. Based on scaling arguments, in Sec. VII the ratios of the energy gains, acceleration lengths, and gradients for a number of laser-driven acceleration mechanisms are summarized in tabular form.

## II. SOLUTIONS OF SCALAR WAVE EQUATION

The scalar wave equation is given by

$$\left(\nabla^2-\frac{1}{c^2}\frac{\partial^2}{\partial t^2}\right)E(x,y,z,t)=0,$$

where $E(x,y,z,t)$ represents a transverse component of the electric field at point $(x,y,z)$ in space and at time $t$. The field can be expressed as

$$E(x,y,z,t)=\tfrac{1}{2}\varepsilon(x,y,z,t)\exp(i\psi_p)+\text{c.c.}, \tag{4}$$

where $\varepsilon$ is the envelope and

$$\psi_p=\beta z-\omega t \tag{5}$$

is the plane-wave phase and $\beta$ is the axial wave number. At this stage one can proceed in various ways depending on the form of $\varepsilon$.

### A. Gaussian beam modes

If $\beta$ is chosen to satisfy the free-space dispersion relation

$$\beta\equiv\omega/c, \tag{6}$$

one can assume that the envelope is a slowly varying function of coordinates and time, in which case substitution of Eq. (4) into the wave equation leads to

$$\left[\nabla_\perp^2+2i\frac{\omega}{c}\left(\frac{\partial}{\partial z}+\frac{1}{c}\frac{\partial}{\partial t}\right)+\frac{\partial^2}{\partial z^2}-\frac{1}{c^2}\frac{\partial^2}{\partial t^2}\right]\varepsilon=0, \tag{7}$$

where $\nabla_\perp$ is the transverse gradient operator. Effecting the change of variables

$$\eta=z-ct,\quad \zeta=z, \tag{8}$$

Eq. (7) reduces to

$$\left(\nabla_\perp^2+2i\frac{\omega}{c}\frac{\partial}{\partial\zeta}+2\frac{\partial^2}{\partial\eta\partial\zeta}+\frac{\partial^2}{\partial\zeta^2}\right)\varepsilon=0. \tag{9}$$

If the typical scale length associated with the transverse variation of the field is $w_0$, it follows that $\nabla_\perp=O(1/w_0)$. Assuming the axial scale length associated with the laser pulse to be $l$, the terms in Eq. (9) are seen to have the following orders of magnitude:

$$\nabla_\perp^2=O(\pi/\lambda Z_R),$$

$$(\omega/c)\partial/\partial\zeta=O(2\pi/\lambda Z_R),$$

$$\partial^2/\partial\zeta\partial\eta=O(1/lZ_R),$$

$$\partial^2/\partial\zeta^2=O(1/Z_R^2).$$

The standard paraxial approximation corresponds to the ordering

$$Z_R,\quad l\gg\lambda, \tag{10}$$

from which Eq. (9) reduces to

$$\left(\nabla_\perp^2+2i\frac{\omega}{c}\frac{\partial}{\partial\zeta}\right)\varepsilon=0. \tag{11}$$

A well-known solution to Eq. (11) is the fundamental Gaussian beam mode [22]

$$\varepsilon(\mathbf{r}) = \varepsilon_0 \frac{w_0}{w} \exp(-r^2/w^2) \exp[i(\psi_0 + \psi_\kappa + \psi_G)], \quad (12)$$

where $r = (x^2 + y^2)^{1/2}$ is the radius in cylindrical coordinates, $\varepsilon_0$ and $\psi_0$ are constants,

$$w(z) = w_0 (1 + z^2/Z_R^2)^{1/2} \quad (13)$$

is the spot size at $z$,

$$\psi_\kappa(z) = (r^2/w^2) z/Z_R \quad (14)$$

is the phase due to the curvature of the wave fronts, and

$$\psi_G(z) = -\tan^{-1}(z/Z_R) \quad (15)$$

is the axial phase shift, due to the Guoy effect, which is present whenever a beam passes through a focus [22]. The fundamental and higher-order Gaussian beam modes are free-space eigenfunctions of the paraxial wave equation and their properties are well known. In particular, a collimated Gaussian beam forms a focus with a minimum spot size (waist) $w_0$ and as it passes through the focus the phase changes by $\pi$ over a distance on the order of $Z_R$. Optical elements with curved surfaces play a special role in the propagation of Gaussian beams or in confining Gaussian beams in optical resonators. When the curvature of these elements (e.g., mirrors or lenses) is matched to the wavefront curvature of the beam, each element will reflect or propagate the beam with little distortion. By choosing the transverse size of the optical element to be large compared to $w(z)$, distortions due diffraction or spillover can be made to be negligible.

### B. Bessel beam modes

A different form for the solution to the wave equation is obtained by assuming that the entire $z$ and $t$ dependence of the solution is contained in the plane-wave phase in Eq. (5) and hence $\varepsilon$ is a function of $x$ and $y$ only. Introducing the *angular spectrum* $A(\varphi)$ of the field [23],

$$\varepsilon(x,y) = \frac{1}{2\pi} \int_0^{2\pi} d\varphi\, A(\varphi) \exp[ik_\perp (x \cos\varphi + y \sin\varphi)] \quad (16)$$

is an *exact* solution of the wave equation provided the transverse wave number $\mathbf{k}_\perp = k_\perp (\mathbf{e}_x \cos\varphi + \mathbf{e}_y \sin\varphi)$ satisfies the dispersion relation

$$\omega^2 = c^2(\beta^2 + k_\perp^2), \quad (17)$$

where $\mathbf{e}_x$ ($\mathbf{e}_y$) is the unit vector along the $x(y)$ axis. Equation (16) is the representation of the beam in terms of a continuous set of infinite plane waves with direction cosines $[(ck_\perp/\omega)\cos\varphi, (ck_\perp/\omega)\sin\varphi, c\beta/\omega]$ [36]. The $x,y$ spatial frequencies are $(k_\perp/2\pi)\cos\varphi, (k_\perp/2\pi)\sin\varphi$. For $k_\perp/\beta \ll 1$, the spatial frequency components are only slightly inclined to the $z$ axis and the electromagnetic field has beamlike characteristics with a dominant direction of propagation.

For an azimuthally symmetric angular spectrum $A(\varphi) = \varepsilon_0 = \text{const}$, Eq. (16) reduces to the fundamental Bessel beam mode [23]

$$\varepsilon(x,y) = \varepsilon_0 J_0(k_\perp t), \quad (18)$$

where $J_0$ is the ordinary Bessel function of the first kind of order zero. The ideal $J_0$ beam has a sharp intensity peak on axis with an infinitely long depth of field of the focal region and thus may be suitable in applications such as precision alignment. It should be noted that an ideal Bessel beam has an infinite number of side lobes around the central peak and, importantly, each lobe carries nearly as much power as the central peak. In any experimental setup, only a clipped Bessel beam can be formed and the central lobe is subject to diffractive spreading, with a finite focal depth [24,28–30]. Nonetheless, the utility of Bessel beams in applications such as laser-driven acceleration is of interest. In the following sections, the particular example of the vacuum beat wave accelerator is considered in detail.

## III. SCALAR DIFFRACTION THEORY

To determine the energy gain when a particle interacts with a laser beam, it is necessary to have expressions for the electromagnetic fields as functions of space and time. Equations (12)–(15) are the necessary forms for a Gaussian beam. Since the corresponding expressions for Bessel beams are not well known, the appropriate formulas are derived in this section.

### A. Huygens-Fresnel formulation

The simplest analytical method is to specify the transverse beam profile in the plane of an aperture and to propagate the beam forward using Huygens' principle. This principle can be expressed as [37]

$$\varepsilon(x,y,z) = \frac{k}{2\pi i} \int_{\text{aperture}} dS' \frac{\exp[ik(R-z)]}{R} \times \left(1 + \frac{i}{kR}\right) \frac{\mathbf{n}\cdot\mathbf{R}}{R} \varepsilon(x',y',z'). \quad (19)$$

Here, $k \equiv \omega/c$, $\mathbf{R}$ is the radius vector from the element of surface integration $dS'$ at $(x',y',z')$ to the point of observation $(x,y,z)$, and $\mathbf{n}$ is a unit vector that is normal to the plane of the aperture and directed towards the observation point. Further, the function $\varepsilon$ in the integrand is assumed to be given on the aperture. The key dependence in Eq. (19) is the phase factor $\exp(ikR)$. For definiteness here, the aperture is taken to be the plane $z' = 0$, from which $\mathbf{n} = \mathbf{e}_z$. In the paraxial limit, $R$ in the exponent may be approximated by

$$R = z + \frac{(x-x')^2 + (y-y')^2}{2z} + \cdots \quad (20)$$

$$\approx z + \frac{r^2}{2z} - \frac{rr'\cos(\theta - \theta')}{z} + \frac{r'^2}{2z}, \quad (21)$$

where $(r,\theta)$ and $(r',\theta')$ denote the polar coordinates at the observation point and at the aperture, respectively. Substituting Eq. (21) into Eq. (19), to leading order, the field at the observation point is given by the Fresnel approximation to Huygens' integral:

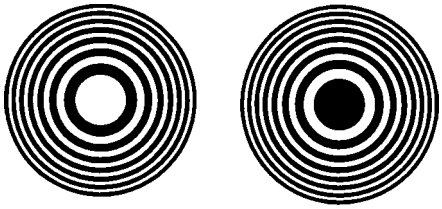

FIG. 2. Fresnel zone plates.

$$\varepsilon(r,\theta,z)\approx\frac{-ik}{2\pi z}\exp(ikr^2/2z)\int_0^a dr' r'\int_0^{2\pi} d\theta'\,\varepsilon(r',\theta')$$
$$\times\exp\{ik[r'^2-2rr'\cos(\theta-\theta')]/2z\}, \qquad (22)$$

where $a$ is the aperture radius.

Equation (22) may be written in a scaled form, permitting useful interpretation [22]. The intensity at an observation point $z=L$ can be imagined to consist of contributions from annular rings on the aperture whose radii $r_n\equiv[(x-x_n')^2+(y-y_n')^2]^{1/2}$ are given by

$$r_n^2=nL\lambda \qquad (23)$$

(Fig. 2), defining Fresnel zones $n=1,2,3,\ldots$. On account of the phase factor in the integrand of Eq. (22), each successive zone makes an equal contribution to the integral, with alternating sign. For an aperture of radius $a$, the number of Fresnel zones $N$ as seen from the observation point $z$ is [22]

$$N\equiv\frac{a^2}{z\lambda} \qquad (24)$$

in terms of which Eq. (22) can be rewritten as

$$\varepsilon\approx -iN\exp[i\pi N(r/a)^2]\int_0^1 d\rho\,\rho\int_0^{2\pi} d\theta'\,\varepsilon(\rho,\theta')$$
$$\times\exp\{i\pi N[\rho^2-2(r/a)\rho\cos(\theta-\theta')]\}, \qquad (25)$$

where $\rho=r'/a$. For an azimuthally symmetric system, the angular integral is readily performed to obtain

$$\int_0^{2\pi} d\theta'\exp[-2\pi iN(r/a)\rho\cos(\theta-\theta')]$$
$$=2\pi J_0[2\pi N(r/a)\rho],$$

and Eq. (25) reduces to

$$\varepsilon(r,z)\approx -2\pi iN\exp[i\pi N(r/a)^2]$$
$$\times\int_0^1 d\rho\,\rho\varepsilon(\rho)J_0[2\pi N(r/a)\rho]$$
$$\times\exp(i\pi N\rho^2). \qquad (26)$$

Observe that the diffraction pattern given by Eq. (26) depends on $z$ only through the Fresnel number. The limit $N\ll 1$ leads to the far-field pattern and for a uniformly illuminated circular aperture one obtains the well-known Airy disk with a dominant central lobe. The near-field pattern, i.e., the limit $N\geqslant 1$, is more complex. For uniform illumination of a circular aperture, the pattern has $N$ large amplitude ripples across the full beam width, with a central peak intensity for $N$ odd and a central null for $N$ even. Thus, the on-axis intensity of a uniformly lit aperture oscillates at an increasing frequency as one moves towards the aperture.

### B. Validity of the Huygens-Fresnel approximation

In writing Eq. (22), a number of approximations have been made. One of these involves the neglect of higher-order terms in the binomial expansion of $R$, Eq. (20). This can be justified provided (i) the neglected quartic terms are small compared to the quadratic terms in Eq. (20) and (ii) the phase variation across the aperture due to the quartic terms is small compared to $\pi/2$. In practical cases, where the aperture is many wavelengths wide, the requirement (ii) is more demanding than (i) and can be expressed in the form

$$\frac{z}{a}\gg\left(\frac{a}{2\lambda}\right)^{1/3}. \qquad (27)$$

Generally, this limitation applies to nonparaxial beams where there are sharp discontinuities in amplitude or in phase. For paraxial beams, however, the validity of the Huygens-Fresnel approximation is not limited by Eq. (27). By direct substitution, one can verify that Eq. (22) is an *exact* solution of the paraxial wave equation, Eq. (11), irrespective of the value of $z$. Since the area of Fresnel zones is proportional to $L$ [Eq. (23)], Eq. (22) remains well-behaved as $L\rightarrow 0$. In fact, Eq. (27) can be viewed as providing an estimate of the distance beyond which an initially nonparaxial beam becomes paraxial [22]. In what follows, only paraxial beams will be considered and Eq. (22) will be assumed to be valid for $z>0$.

## IV. GENERATION OF BESSEL BEAMS

The angular spectrum representation in Eq. (16) helps one devise means for generating Bessel beam modes. The purpose of this section is to examine three methods of generating Bessel beams: (i) a circular slit, (ii) a holographic optical element, and (iii) an axicon. The aim of the analysis is to derive expressions for the electric field for these configurations and obtain the form for the axial phase shift in each case.

### A. Circular slit

Consider a narrow circular slit of mean diameter $d$ placed in the back focal plane of a thin lens of focal length $f$ and illuminated by a coherent plane wave of uniform intensity, as shown in Fig. 3 [23,38]. The slit acts as a source of waves and the lens collects the spatial frequencies whose wave vectors lie on the surface of a cone with half-apex angle $\vartheta=\tan^{-1}[d/(2f)]$ and $k_\perp=(\omega/c)\sin\vartheta$. If $R$ is the radius of the lens, the spatial frequencies overlap and form a line focus that extends a distance $Z_{\rm slit}=R/\tan\vartheta\approx 2fR/d$ ($\vartheta\ll 1$).

To demonstrate that this system forms a Bessel beam, one takes the field just after the slit to be given in terms a $\delta$ function, $\varepsilon=\varepsilon_0(d/2)\delta(r-d/2)$. Making use of Eq. (26), this input field can be propagated to obtain the field at the surface of the lens,

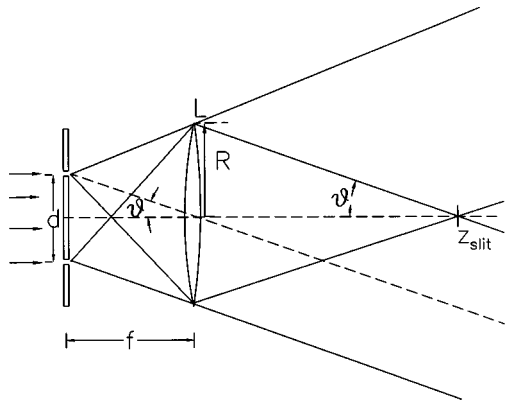


FIG. 3. Bessel beam formed by illuminated circular slit placed in back focal plane of lens of focal length $f$ and radius $R$. Mean diameter of slit is $d$; $Z_{\rm slit}$ is propagation distance of Bessel beam.

$$\varepsilon(r,f)\approx\frac{-ik}{f}\varepsilon_0(d/2)^2 \times\exp\{ik[r^2+(d/2)^2]/2f\}J_0[krd/(2f)]. \tag{28}$$

On passing through the lens, the wave fronts experience a phase delay equal to [39]

$$\Delta\psi_{\rm lens}(r)=\frac{k}{2f}(R^2-r^2), \tag{29}$$

whose effect on the wave in Eq. (28) is equivalent to multiplication by a complex-valued transmission function $t_{\rm lens}(r)=\exp[i\Delta\psi_{\rm lens}(r)]$. Thus the lens exactly cancels the quadratic phase curvature in Eq. (28), leading to a Bessel beam with intensity distribution $\propto J_0^2[krd/(2f)]$.

For comparison with a Gaussian beam, it is tempting to evaluate a Rayleigh range for the Bessel beam by taking the waist to be equal to the radius of the *central* spot; i.e., $w_0\approx 1/k_\perp$ [see Eq. (18)]. It follows that $Z_R=\pi w_0^2/\lambda\approx\pi w_0/(k_\perp\lambda)\approx w_0/2\sin\vartheta$, from which $Z_{\rm slit}\gg Z_R$ since $R\gg w_0$. Thus with appropriate choices for the slit and lens parameters one can arrange for $Z_{\rm slit}$ to exceed $Z_R$ significantly, apparently beating the diffraction of Gaussian beams. Experiments in support of this conjecture were performed in 1987, demonstrating a nearly constant intensity from the lens out to a distance $\sim Z_{\rm slit}$ [23]. Since then, Bessel beams have been the subject of much theoretical analysis and experimental study as a paradigm of what are referred to as ''diffraction-free'' beams [28–30,40]. However, the designation ''diffraction-free'' is inappropriate [24,28,29]. Briefly, a Bessel beam propagates out to a distance equal to $Z_{\rm slit}\approx R/\tan\vartheta$ because the adjacent side lobes feed energy into the central lobe. If the side lobes are clipped, by reducing the lens radius to $w_0$, the Bessel beam would propagate no further than a Gaussian beam of waist $w_0$. In other words, for a fair comparison it is necessary to take a Gaussian beam with the same transverse extent as the full Bessel beam (and not just the central lobe of the beam). If this is done, careful comparison of a Bessel beam with a Gaussian beam reveals that the latter has, in fact, a better energy transfer capability [28,29].

### B. Holographic optical element

A uniformly illuminated thin slit in an opaque screen is clearly an inefficient means of generating Bessel beams due to the severe loss of light. A holographic optical element (HOE) can also generate Bessel beams, offering the potential of 100% transmission efficiency while at the same time doubling the depth of field of the focal region. To analyze the effect of an HOE, it is necessary to first recall the optical properties of Fresnel zone plates [41].

Refer to Eq. (23) for the radius of the $n$th Fresnel zone (Fig. 2), consider a uniformly illuminated transparent disk and recall that the contribution from one zone is nearly canceled by that from the next. Clearly the intensity of the radiation emerging from this disk will increase significantly if either the even- or the odd-numbered zones are blocked out. Consider now a point source $S$ on the $z$ axis at a distance $u$ from a zone plate. By considering the optical path difference between the direct ray to a point $P$ at a distance $v$ past the plate and the ray through the $n$th zone, it can be shown that [41]

$$\frac{1}{u}+\frac{1}{v}=\frac{1}{r_n^2/n\lambda}, \tag{30}$$

which is the usual formula for a lens with (primary) focal length $f_1=r_n^2/n\lambda$. Thus the source $S$ is imaged by converging *diffracted* light at the image point $P$. Zone plates are used to image atoms [42], $\alpha$ particles, as well as short-wavelength radiation, such as x rays, for which ordinary refraction is negligible [43]. A common means for making zone plates is to draw a large-scale version with a high-quality laser printer that is then photographically reduced.

When light is scattered from a small object and then interferes with a reference beam, zone plate fringes are formed. For an extended object each point generates its own fringe pattern and the collection of the overlapping zone plate fringes is a recording of a hologram. As discussed in connection with Eq. (30), a zone plate functions somewhat like a lens in that it diffracts collimated light to a converging focal point. Thus when the hologram is read, by illuminating it with light, the constituent zone plates form images that combine to reconstitute the object.

An HOE is a device consisting of a fringe pattern and can function as a complex lens system. It can be created by actual interferometry or by a computer-controlled plotter simulating an interference pattern. Bessel beams have been produced by using HOE's that consist of a series of concentric circles, Fig. 4, with a constant radius increment from one circle to the next [25]. Ideally, the effect of the hologram on the incident wave can be represented by a multiplicative transmission function $t_{\rm holo}(r)=\exp[i\Delta\psi_{\rm holo}(r)]$, where

$$\Delta\psi_{\rm holo}(r)=-2\pi r/r_0, \tag{31}$$

and $r_0=$const is the hologram fringe spacing. Inserting this transmission function into Eq. (22), one obtains

$$\varepsilon(r,z)\approx\frac{-ik}{z}\varepsilon_0\exp(ikr^2/2z)\int_0^a dr'r'J_0(krr'/z) \times\exp[i(kr'^2/2z-2\pi r'/r_0)], \tag{32}$$

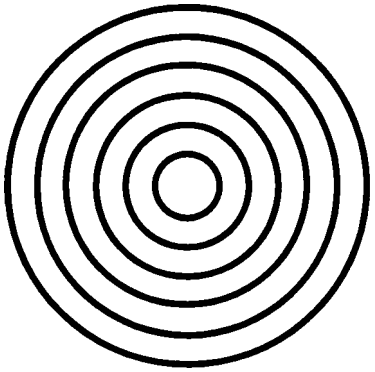

FIG. 4. Hologram for generating Bessel beam.

where $a$ is now the hologram radius. Equation (32) may be simply evaluated by making use of the method of stationary phase. Assuming the exponential in Eq. (32) is the most rapidly varying factor, the phase

$$\psi_{\rm int} \equiv kr'^2/2z - 2\pi r'/r_0 \tag{33}$$

is stationary at

$$r_s' = 2\pi z/(kr_0), \quad r_s' < a. \tag{34}$$

Observe that there is no stationary phase point when $z$ is large enough that $r_s' > a$. Thus

$$\varepsilon(r,z) \approx \frac{-2\pi i}{r_0}\varepsilon_0 J_0(2\pi r/r_0) \times \exp[i(kr^2/2z - \pi\lambda z/r_0^2)][1 - H(z - ar_0/\lambda)], \tag{35}$$

where $H(\,)$ is the Heaviside unit step function. The first and second terms in the exponential factor in Eq. (35) represent the curvature and Guoy phase, respectively, for the HOE. Omitting multiplicative constants, the time-averaged intensity distribution is

$$I(r,z) \equiv |\varepsilon(r,z)|^2 = (2\pi/r_0)^2 \varepsilon_0^2 J_0^2(2\pi r/r_0)[1 - H(z - ar_0/\lambda)], \tag{36}$$

i.e., the ubiquitous Bessel beam distribution. Observe that the propagation distance of the Bessel beam in Eq. (36) is

$$Z_{\rm HOE} = ar_0/\lambda. \tag{37}$$

Writing $r_0 = a/N_f$, where $N_f$ is the number of fringes on the HOE, Eq. (37) becomes

$$Z_{\rm HOE} = a^2/N_f\lambda. \tag{38}$$

This is identical to the primary focal length in Eq. (30) for a Fresnel zone with $N_f$ zones. Equation (38) clearly demonstrates that the propagation distance of the beam is a characteristic of the HOE employed in generating the beam [30]. The propagation distance in Eq. (38) is in excellent agreement with experimental observations [25].

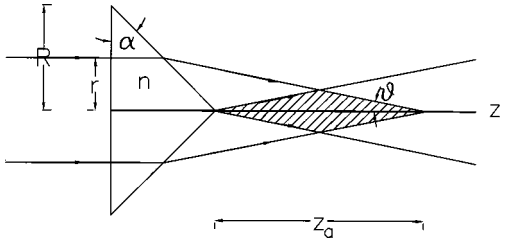


FIG. 5. Simple axicon optical element for generating Bessel beam, showing ray incident at radius $r$. Refractive index of axicon material is $n$, base radius is $R$, and $Z_a$ is depth of field of focal region.

The simplest method to realize the HOE phase function is to record the HOE in a binary-amplitude form. Diffraction efficiency of such an HOE is low. The efficiency improves substantially if the binary-amplitude structure is replaced with a binary-phase structure. Using lithographic methods, multiphase holograms with efficiencies approaching 100% can be fabricated [25].

### C. Axicon

An axicon is an optical element that forms a line image of a small source [44]. A Bessel beam can be easily formed with high conversion efficiency with the use of an axicon. Axicons can be utilized in applications such as precision alignment, materials processing, writing, and scribing [27,31]. Additionally, they can be used to obtain continuous extended sparks in gases [45,46] and long-thin optically pumped plasmas in excited states suitable for laser gain [47]. The utility of axicon optical elements in the context of laser-driven accelerators has also been noted [10,14,15].

Referring to Fig. 5, one can obtain an expression for the extent of the line focus based on purely geometrical optics considerations. Applying Snel's law to refraction of a ray at the inclined face of the axicon, one obtains

$$n \sin\alpha = \sin(\vartheta + \alpha), \tag{39}$$

where $n$ is the refractive index and $\alpha$ is the angle indicated in Fig. 5. For a ray incident at radius $r$, the line focus extends from the apex out to a distance $Z_a$, where

$$Z_a = r(\cot\vartheta - \tan\alpha). \tag{40}$$

To obtain the electric field distribution in the image plane, consider the ray $QQ'P$ that is incident on the plane face of the axicon at a radial distance $r'$ from the $z$ axis, as shown in Fig. 6. The ray emerges from the axicon at the point $Q'$ with

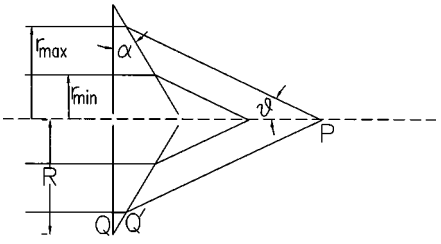


FIG. 6. Details of axicon optical element for evaluation of electromagnetic field using Huygens' principle.

coordinates $(r',\theta',z_0)$ and propagates to the observation point $P$ with coordinates $(r,\theta,z)$. The optical path length $[QQ'P]$ can be written as

$$[QQ'P]=nz_0+[(z-z_0)^2+r^2+r'^2-2rr'\cos(\theta-\theta')]^{1/2}$$
$$\approx z+(n-1)z_0-\frac{rr'}{z-z_0}\cos(\theta-\theta')+\frac{1}{2}\frac{r^2+r'^2}{z-z_0}, \tag{41}$$

where $z_0$ can be written in terms of the axicon radius $R$ as

$$z_0=(1-r'/R)R\tan\alpha. \tag{42}$$

For an annular beam with uniform intensity in $R_{\min}<r'<R_{\max}$, Eq. (19) reduces to

$$\varepsilon(P)\approx -ik\varepsilon_0 \times\exp[ik(n-1)R\tan\alpha] \times\int_{R_{\min}}^{R_{\max}}\frac{dr'r'}{z+(n-1)(R-r')\tan\alpha} \times J_0\left[\frac{krr'}{z-(R-r')\tan\alpha}\right] \times\exp\left\{ik\left[\frac{(r^2+r'^2)/2}{z-(R-r')\tan\alpha}-(n-1)r'\tan\alpha\right]\right\}. \tag{43}$$

For asymptotic evaluation of the integral in Eq. (43), one finds that the stationary phase point is located at $r'=z(n-1)\tan\alpha$, from which

$$\varepsilon(P)\approx\varepsilon_0\exp(-i\pi/4)\sqrt{2\pi kz}(n-1) \times\tan\alpha J_0[kr(n-1)\tan\alpha] \times\exp[ik(n-1)R\tan\alpha] \times\exp\left\{i\frac{k}{2}[r^2/z-z(n-1)^2\tan^2\alpha]\right\} \times\{H[z(n-1)\tan\alpha-R_{\min}] -H[z(n-1)\tan\alpha-R_{\max}]\}. \tag{44}$$

Observe that the field amplitude in Eq. (44) is proportional to $(n-1)\tan\alpha$. The limit $n\to 1$ or $\alpha\to 0$ corresponds to no axicon in the path of the incident light.

For the axicon beam, the all-important axial phase shift is given by $-kz(n-1)^2\tan^2\alpha/2$ in the second exponent of Eq. (44). This is analogous to the phase shift $-\tan^{-1}(z/Z_R)$ in Eq. (15) for the Gaussian beam and $-\pi\lambda z/r_0^2$ in the exponent of Eq. (35) for the HOE. A cumulative axial phase shift is expected to emerge whenever radiation beams pass through a focus [22].

## V. VACUUM BEAT WAVE ACCELERATION

The purpose of this section is to take the example of the vacuum beat wave accelerator (VBWA), evaluate the energy gain, and compare the result for Gaussian beams with that for Bessel beams. Acceleration and bunching of electrons with two Gaussian laser beams with differing frequencies has been analyzed in depth elsewhere [11,13,48]. The key idea in the VBWA concept is that by appropriate choice of parameters, the Guoy phase shifts of the individual laser beams can be made to cancel out in the $\mathbf{v}\times\mathbf{B}$ force. Thus, while the individual laser beams are superluminous, the beat wave is luminous and can be near-synchronous with particles. For brevity, an outline of the derivation of the expression for the energy gain will be presented, referring the reader to Ref. [13] for details.

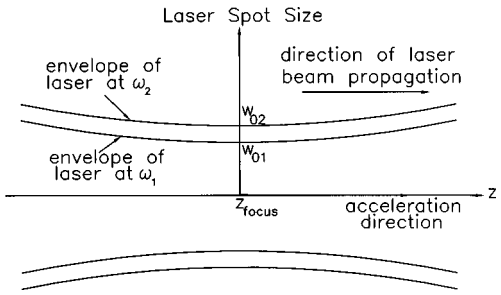


FIG. 7. Schematic of vacuum beat wave accelerator configuration driven by two collinear and copropagating Gaussian laser beams coming to a common focus at $Z_{\text{focus}}$. The waist of the laser beam of frequency $\omega_1$ ($\omega_2$) is $w_{0,1}$ ($w_{0,2}$).

### A. VBWA with Gaussian beams

Figure 7 is a schematic of the VBWA configuration driven by Gaussian beams. To conform to Ref. [13], the vector potential of each circularly polarized laser beam (indicated by suffix $j=1,2$) is written in a form that is similar to Eqs. (4) and (12), i.e.,

$$\mathbf{A}_j=\frac{A_{0j}w_{0j}}{w_j}\exp(-r^2/w_j^2)(\mathbf{e}_x\cos\psi_j+\mathbf{e}_y\sin\psi_j)+A_{zj}\mathbf{e}_z, \tag{45}$$

where

$$\psi_j=\psi_{pj}+\psi_{Gj}+\psi_{kj}+\psi_{0j} \tag{46}$$

is the phase, $\lambda_j$ is the wavelength, $Z_{Rj}=\pi w_{0j}^2/\lambda_j$ is the Rayleigh range for the beam with waist $w_{j0}$, $A_{0j},\psi_{0j}$ are constants, and $\mathbf{e}_x,\mathbf{e}_y,\mathbf{e}_z$ are unit vectors. The plane-wave phase, spot size, curvature phase, and Guoy phase in Eqs. (45) and (46) are given by Eqs. (5) and (13)–(15), respectively, with appropriate juxtaposition of the suffix $j$.

The rate of change of the relativistic factor $\gamma$ can be expressed as

$$\frac{d\gamma}{dz}\approx\frac{(k_2-k_1)\hat{a}_1\hat{a}_2}{(p_z/mc)}\sin(\psi_2-\psi_1), \tag{47}$$

where $k_j=2\pi/\lambda_j$ is the wave number, $\hat{a}_j=(a_{0j}w_{0j}/w_j)\exp(-r^2/w_j^2)$, $a_{0j}=|e|A_{0j}/(mc^2)$ is the normalized vector potential, $\gamma=[1+(p_x/mc)^2+(p_y/mc)^2+(p_x/mc)^2]^{1/2}$, and $p_{x,y,z}$ is the $x,y,z$ component of the momentum. Equation (47) is based on the assumption that the change in the energy is predominantly due to interaction with

the slowly varying beat wave, via the $\mathbf{v}\times\mathbf{B}$ force, rather than direct interaction with the electric field of the laser beams [11,13].

The equation of motion for the phase difference $\psi_2-\psi_1$ is given by

$$\frac{d(\psi_2-\psi_1)}{dz}=(k_2-k_1)(\beta_{\rm ph}^{-1}-\beta_z^{-1})+\frac{2\beta_\perp\cdot\mathbf{r}}{\beta_z}(z-Z_{\rm focus})\times\left(\frac{1}{Z_{R2}w_2^2}-\frac{1}{Z_{R1}w_1^2}\right), \tag{48}$$

where $\beta_{\rm ph}$, the beat wave phase velocity normalized to $c$, is given by

$$\beta_{\rm ph}^{-1}=1-\frac{1-(1-\hat{z}_2^2)r^2/w_2^2}{(k_2-k_1)Z_{R2}(1+\hat{z}_2^2)}+\frac{1-(1-\hat{z}_1^2)r^2/w_1^2}{(k_2-k_1)Z_{R1}(1+\hat{z}_1^2)}, \tag{49}$$

$\hat{z}_j=(z-Z_{\rm focus})/Z_{Rj}$, $Z_{\rm focus}$ is the (common) focal point of the two laser beams, $\beta=(\beta_\perp,\beta_z)=\mathbf{v}/c$ is the particle velocity normalized to $c$, and $\mathbf{r}$ is the radius vector to the particle.

In Ref. [13], several limits of the interaction of particles with the beat wave generated by two Gaussian laser beams were examined. If, for simplicity, one considers the case of a synchronous interaction with two laser beams, the change in energy $W^{(G)}\equiv mc^2\int dz(d\gamma/dz)$ may be written as

$$W^{(G)}=\pi\gamma^{-1}(k_2-k_1)Z_R a_{0,1}^{(G)}a_{0,2}^{(G)}\sin\psi_{\rm syn}, \tag{50}$$

where, in practical units, for a Gaussian beam

$$a_{0j}^{(G)}=\left[\frac{P_j\,({\rm TW})}{0.0432}\right]^{1/2}\frac{\lambda_j}{w_{0j}}. \tag{51}$$

In Eq. (51), $P_j$(TW) is the laser beam power in TW. Equation (50) is appropriate for the case where the Rayleigh ranges of the two beams coincide, i.e., $Z_{R1}=Z_{R2}\equiv Z_R$. The case of equal Rayleigh ranges is of interest since it ensures that the Guoy phase shifts of the two laser beams cancel in the $\mathbf{v}\times\mathbf{B}$ force. Moreover, it follows from Eq. (49) that the equality of the Rayleigh ranges implies that the on-axis phase velocity of the beat wave is constant and equal to $c$. Thus it is plausible to assume that the particle maintains a constant phase $\psi_{\rm syn}\equiv\psi_2-\psi_1$ relative to the beat wave provided its transverse excursions are negligible. (In the simulation results to be presented later, these assumptions are not made.)

### B. VBWA with Bessel beams

Figure 8 depicts a possible VBWA arrangement employing a compound axicon focusing element that is configured to permit an overlap region for the two laser beams. The incident laser beams are assumed to be annular, with the lower frequency beam surrounding the higher frequency beam. To generalize Eq. (40) to annular beams, it is useful to define

$$z_{\min j}=\frac{r_{\min j}}{\tan\vartheta_j}+(R_j-r_{\min j})\tan\alpha_j+R_{1+\delta_{j,1}}\tan\alpha_1, \tag{52}$$

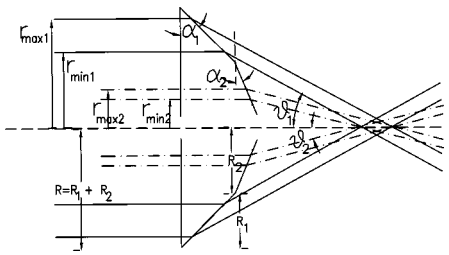


FIG. 8. Vacuum beat wave accelerator configuration driven by two collinear and copropagating Bessel laser beams formed by compound axicon. Incident beams are annular, uniformly illuminating regions $r_{\min 1}<r<r_{\max 1}$ with laser beam 1 and $r_{\min 2}<r<r_{\max 2}$ with laser beam 2.

$$z_{\max j}=\frac{r_{\max j}}{\tan\vartheta_j}+(R_j-r_{\max j})\tan\alpha_j+R_{1+\delta_{j,1}}\tan\alpha_1, \tag{53}$$

as the minimum and maximum axial locations—within geometrical optics—of the $j$th annular beam, respectively. Here $r_{\max j}$ ($r_{\min j}$) is the outer (inner) radius of the $j$th beam in the incidence plane, $R=R_1+R_2$ is the radius of the axicon base, the angles $\vartheta_j$ and $\alpha_j$ are indicated in Fig. 8, and $\delta_{j,1}$ is the Kronecker delta. Subtracting Eq. (52) from Eq. (53), the axial extent of the $j$th beam in Fig. 8 is given by

$$Z_{aj}=(r_{\max j}-r_{\min j})(\cot\vartheta_j-\tan\alpha_j). \tag{54}$$

The equation of motion for the evolution of the phase difference in the Bessel beam beat wave is given by

$$\frac{d(\psi_2-\psi_1)}{dz}=(k_2-k_1)\left(\beta_{\rm ph}^{-1}-\beta_z^{-1}+\frac{dr^2}{dz^2}\right), \tag{55}$$

where, making use of Eq. (44), the normalized Bessel beam beat wave phase velocity is given by

$$\beta_{\rm ph}^{-1}=1-\frac{(n-1)^2}{2}\frac{\omega_2\tan^2\alpha_2-\omega_1\tan^2\alpha_1}{\omega_2-\omega_1}-\frac{r^2}{2z^2}. \tag{56}$$

For comparison with Eq. (50), $\beta_{\rm ph}=1$ in Eq. (55) (for $r=0$) provided

$$\frac{\tan\alpha_1}{\tan\alpha_2}=\left(\frac{\omega_2}{\omega_1}\right)^{1/2}, \tag{57}$$

or, making use of Eq. (39) for small angles,

$$\frac{\vartheta_1}{\vartheta_2}\approx\left(\frac{\omega_2}{\omega_1}\right)^{1/2}. \tag{58}$$

The choice in Eq. (57) ensures that the Guoy phase shifts of the two laser beams cancel in the $\mathbf{v}\times\mathbf{B}$ force. Thus, for a synchronous interaction with $\psi_{\rm syn}\equiv\psi_2-\psi_1=$const, the change in energy for a Bessel beam driven VBWA is

$$W^{(B)}=\pi\gamma^{-1}(k_2-k_1)(z_{\max}^2-z_{\min}^2)F\sin\psi_{\rm syn}, \tag{59}$$

where

$$F = a_{0,1}^{(B)} a_{0,2}^{(B)} \sqrt{k_2 k_1} (n-1)^2 \tan\alpha_1 J_0[k_1 r(n-1)\tan\alpha_1] \times \tan\alpha_2 J_0[k_2 r(n-1)\tan\alpha_2], \quad (60)$$

$$a_{0j}^{(B)} = \left[\frac{P_j\,(\mathrm{TW})}{0.0864}\right]^{1/2} \frac{\lambda_j}{\Delta r_j}, \quad (61)$$

and

$$\Delta r_j = (r_{\max j}^2 - r_{\min j}^2)^{1/2}. \quad (62)$$

In writing Eq. (59), it is assumed that the axicon angles and incident beam dimensions are such that the two Bessel beams overlap on the $z$ axis in the range $z_{\min} < z < z_{\max}$. This will be the case for the simulations in the next section.

### C. Comparison of Gaussian and Bessel beam driven VBWA

The VBWA driven by the two laser beam profiles may be compared by evaluating the ratio $W^{(B)}/W^{(G)}$. Making use of Eqs. (50) and (59), one finds, for small $\alpha_j$,

$$\frac{W^{(B)}}{W^{(G)}} = (n-1)^2 \tan\alpha_1 \tan\alpha_2 \frac{(z_{\max}^2 - z_{\min}^2)}{\Delta r_1 \Delta r_2}, \quad (63)$$

provided the product $P_1 P_2$ is the same for the Gaussian and Bessel beams. For small angles, making use of Eqs. (52), (53), and (57), one finds the remarkable result

$$W^{(B)}/W^{(G)} = 1. \quad (64)$$

Thus, within the limits of the approximations made, a Gaussian beam driven VBWA is as efficient as a Bessel beam driven VBWA. Physically, the reason for this is that a longer interaction length in the Bessel beam case is obtained at the expense of reduced field amplitude. However, in the following section it will be shown, by full-scale numerical simulations that allow transverse excursions of the particles as well as the full complement of the electromagnetic fields, that $W^{(G)}/W^{(B)} \sim 2-3$ in a particular example.

## VI. NUMERICAL RESULTS

Based on the analytical model developed in Sec. V, it appears that a VBWA driven by Bessel beams has the same energy gain as that driven by Gaussian beams. As noted in the preceding section, the analytical model used for this comparison is highly simplified. One can always choose parameters such that the Guoy phase shifts of the two laser beams cancel out in the $\mathbf{v}\times\mathbf{B}$ force on a particle moving along the $z$ axis, allowing synchronous interaction. However, the model neglects transverse displacements of the particles—that can lead to detuning—and retains only the second-order, $\mathbf{v}\times\mathbf{B}$, driving term. In this section, numerical simulations of the two cases are presented, avoiding the analytical simplifications. The numerical method makes use of a leapfrog integrator to push particles in the prescribed fields of the laser beams. The fully relativistic Lorentz equations of motion, including *all* the field components, are solved on the fast temporal and spatial scales, with no averaging. The particle equations of motion are integrated in the speed-of-light coordinate system, with independent variables $\zeta = ct - z$ and $\tau = t$. Boris' rotation is used for accurate finite differencing of the $\mathbf{v}\times\mathbf{B}$ force [49]. For the Gaussian case, the code makes use of Eqs. (45) and (46) for each of the prescribed laser beams. For the Bessel beam case, the laser fields are obtained from Eq. (44) in the region defined by Eq. (54).

TABLE I. Parameters for Gaussian beam driven vacuum beat wave accelerator.

| | |
|---|---|
| Injection energy | 4.5 MeV |
| Normalized emittance | 1.2 $\pi$ mm mrad |
| Particle beam waist | 4 $\mu$m |
| Wavelength $\lambda_1$ | 1 $\mu$m |
| Laser beam waist $w_{0,1}$ | 4 $\mu$m |
| Rayleigh range $Z_{R1}$ | 50 $\mu$m |
| Power (1-$\mu$m beam) $P_1$ | 1.5 TW |
| Power (1/2-$\mu$m beam) $P_2$ | 3 TW |
| Normalized vector potential $a_{0,1}$ | 1.48 |
| Vector potential ratio $a_{0,2}/a_{0,1}$ | 1 |
| Waist ratio $w_{0,2}/w_{0,1}$ | $1/\sqrt{2}$ |

The simulation results are for two laser beams, one at 1 $\mu$m and the other frequency-doubled to 1/2 $\mu$m. A 4.5-MeV beam (represented by 4000 macroparticles) is injected upstream with finite emittance, coming to a focus in the interaction region. Two cases are compared: **A**, a Gaussian beam driven VBWA, and **B**, a Bessel beam driven VBWA. To compare similar cases, the power in the laser beams is the same for the two cases. This implies that the field strength (i.e., the vector potential) in case **B** is small compared to that in case **A**.

### A. Gaussian beams

Table I lists the parameters for the Gaussian beam driven VBWA. In this case, the particle beam is arranged to form a waist (minimum spot size) that is equal to that of the 1-$\mu$m laser beam. The (unperturbed) particle and two laser beams have a common focal point, i.e., all three form a waist at the same $z$ location. Figure 9(a) shows the peak energy and Fig. 9(b) shows the centroid radius as functions of the normalized axial distance $z/Z_{R1}$, where $Z_{R1}$ is the (common) Rayleigh range of the two laser beams. The particles start out 40 Rayleigh ranges upstream of the laser beam foci and are followed to 40 Rayleigh ranges downstream, i.e., the interaction region is in the vicinity of $z/Z_{R1} = 40$ in Fig. 9. The peak energy of the beam after the interaction is observed to be 18 MeV. To put the transverse displacement in perspective, the divergence angle in Fig. 9(b) is relatively small, $\sim$7 mrad. Figures 9(c) and 9(d) are the radial and axial phase-space plots at the end of the run ($c\tau = 0.4$ cm). The phase-space plots show a relatively large spread in the particle distribution, indicating a lack of strong trapping in the VBWA, although it should be noted that at this time ($c\tau = 0.4$ cm) the laser beams have completely diffracted away. Figures 9(e) and 9(f) show the $x$-$y$ and the $\zeta$-$v_x/c$ phase-space plots, respectively, at $c\tau = 0.3$ cm. The $x$-$y$ phase-space plot shows a nearly azimuthally symmetric distribution of particles that is partially hollowed out due to scattering. Figure 9(f) shows a beam of particles emerging from the interaction and propagating towards the left with a relatively narrow distribution, lying inside a cone with half-angle $\sim$0.1 rad.

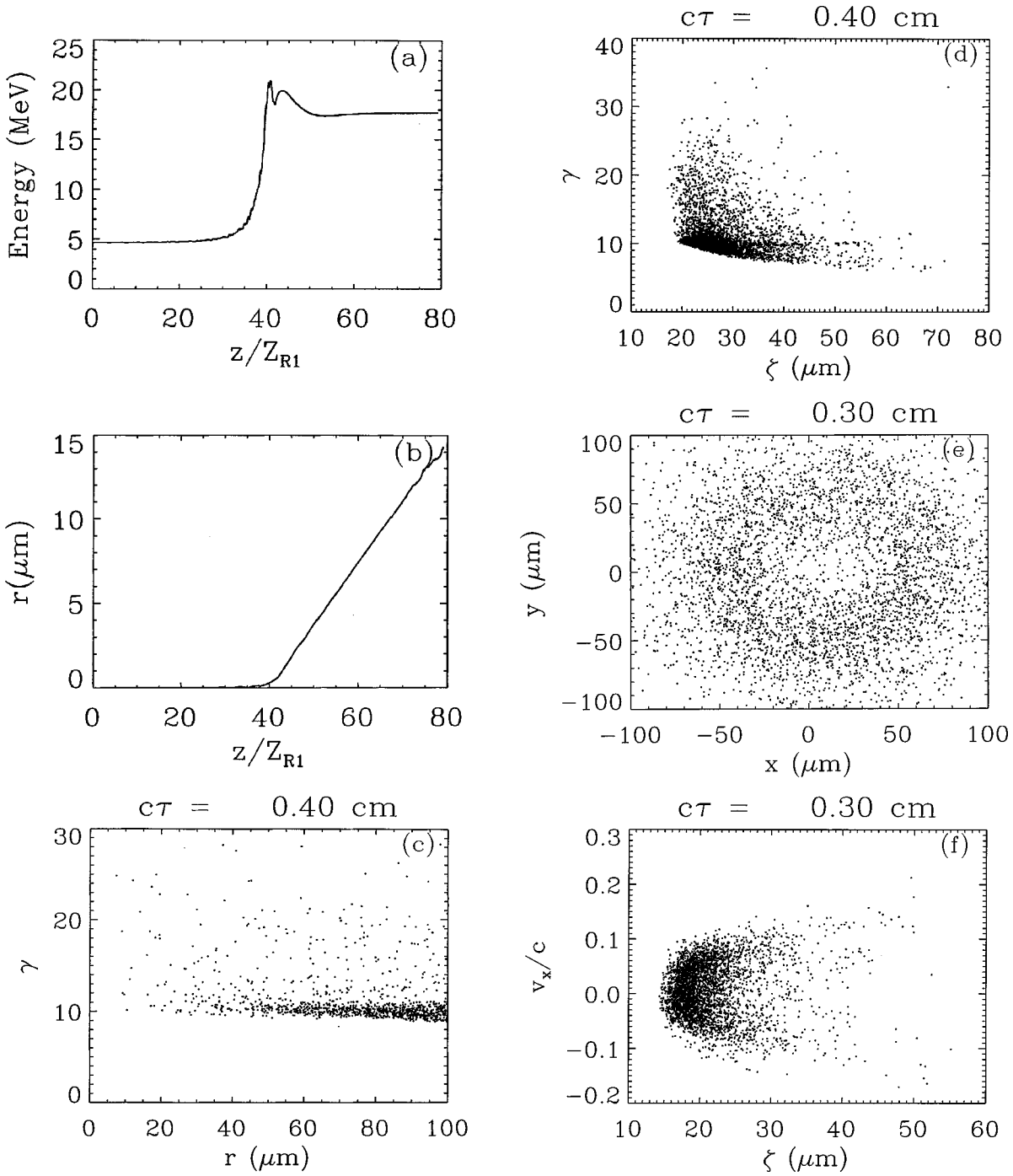


FIG. 9. Simulation results for VBWA driven by Gaussian laser beams, employing initially converging 4.5-MeV finite-emittance particle beam. Particles are injected at $z=0,40$ Rayleigh ranges (40 $Z_{R1}$) upstream of the (common) laser beam foci. Plots of (a) peak energy, (b) centroid radius are shown as functions of $z/Z_{R1}$, while (c) and (d) show radial and axial phase-space plots at end of run, $c\tau=0.4$. The $x$-$y$ and $\zeta$-$v_x/c$ plots, (e) and (f), respectively, are at $c\tau=0.3$.

### B. Bessel beams

Table II lists the parameters for the Bessel beam driven VBWA. The axicon material is taken to be ZnSe, with the refractive index $n=2.6$ assumed to be the same for both the 1- and the $\frac{1}{2}$-$\mu$m light. While not necessarily optimal, the relatively large refractive index allows the use of a thin axicon for a given configuration. The length of the overlap region is 2.58 mm; as a result of this long interaction length, the normalized vector potential in Table II is much less than that for the Gaussian beam case in Table I. The particles start out well before the axicon beams form a line focus and the (unperturbed) particle beam is arranged to have a waist of 4 $\mu$m halfway along the line focus. For comparison, the radii of the central lobes of the Bessel beams measure 7.751 and 5.481 $\mu$m, respectively, for the 1- and 1/2-$\mu$m light. Figure 10(a) shows the peak energy while Fig. 10(b) shows the centroid radius as functions of the normalized axial distance $z/Z_{R1}$, where, for ease of comparison, $Z_{R1}$ has the same numerical value as in Figs. 9(a) and 9(b). The region around the axis where the annular beams form a focus is well-

TABLE II. Parameters for Bessel beam driven vacuum beat wave accelerator.

| | |
|---|---|
| Injection energy | 4.5 MeV |
| Normalized emittance | 1.2 $\pi$ mm mrad |
| Particle beam waist | 4 $\mu$m |
| Wavelength $\lambda_1$ | 1 $\mu$m |
| Power (1-$\mu$m beam) $P_1$ | 1.5 TW |
| Power (1/2-$\mu$m beam) $P_2$ | 3 TW |
| Normalized vector potential $a_{0,1}$ | 0.01 |
| Vector potential ratio $a_{0,2}/a_{0,1}$ | 1 |
| $\alpha_2=\alpha_2/\sqrt{2}$ | 1.25° |
| $\vartheta_2=\vartheta_1/\sqrt{2}$ | 2° |
| $r_{\min,2}=r_{\min,1}/\sqrt{2}$ | 0.405 mm |
| $r_{\max,2}=r_{\max,1}/\sqrt{2}$ | 0.495 mm |

defined with relatively sharp boundaries. As a consequence, the peak energy in Fig. 10(a) rises rapidly as the electron beam enters the overlap region. The peak energy of the beam after the interaction is about 7 MeV. There is a small drop in energy for $z/Z_{R1}>350$; this is an artifact of radial walk-off of some of the high-energy particles. Comparing Figs. 9(a) and 10(a), it may be concluded that the final energy for the Bessel beam driven VBWA is a factor 2–3 less than the Gaussian beam case. Figures 10(c) and 10(d) display the radial and axial phase spaces at the end of the run ($c\tau=2$ cm). As with the Gaussian case, the phase-space plots show a relatively large spread in the particle distribution since the laser beams have long diffracted away. Finally, Figs. 10(e) and 10(f) show the $x$-$y$ and the $\zeta$-$v_x/c$ phase-space plots, respectively, at $c\tau=1.5$ cm. The $x$-$y$ phase-space plot shows a nearly uniform distribution of particles. Note that, unlike the Gaussian-driven VBWA case in Fig. 9(e), the distribution is not hollowed out. Figure 10(f) shows a beam of particles emerging from the interaction and propagating towards the left with a relatively narrow distribution, lying inside a cone with half-angle $\sim$0.1 rad.

## VII. DISCUSSION AND CONCLUSIONS

Laser-driven accelerators are typically characterized by very large acceleration gradients. Diffraction of laser beams, however, imposes a serious limitation on many of these schemes by restricting the interaction length. Additionally, on passing through a focal region a beam undergoes a Guoy phase shift that detunes the wave-particle interaction. The scale length for the diffraction and phase shift of a beam of electromagnetic radiation depends on the transverse profile of the beam. Ordinarily, laser beams are formed by conventional optical elements and have a Gaussian transverse profile. Other optical elements, such as axicons and zone plates (holograms), form beams whose transverse profile is a Bessel function. Based on Huygens' principle, expressions for the electromagnetic field of a Bessel beam that is formed by an axicon illuminated by an annular laser beam have been obtained. These expressions are used to derive and compare the energy gain with that for a Gaussian beam driven vacuum beat wave accelerator. In the VBWA, the Guoy phase of the two laser beams can be canceled out by proper choice of parameters, leading to a beat wave with a phase velocity equal to $c$. An analytical model—neglecting detuning, transverse displacements of the particles, and including the $\mathbf{v}\times\mathbf{B}$ interaction only—predicts equal energy gains for the two configurations. Full-scale, finite emittance particle simulations show that in practice the energy gain for the Bessel beam driven vacuum beat wave accelerator is a factor 2–3 less than that for a Gaussian beam driven configuration. The particle beam emerging from the interaction is, in both cases, nearly azimuthally symmetric, with a relatively small angular divergence. The difference between the analytical prediction and the simulation results for the energy gain can be due to several reasons, e.g., neglect of transverse particle displacement in the analysis. Figures 9(b) and 10(b) show that high-energy particles can wander off the $z$ axis to distances beyond the radial scale length of the laser beam, where the Gaussian and the Bessel beam profiles are quite different. Radial displacements also affect the wave-particle phase relationship that can, over an extended interaction distance, lead to significant differences between the energy gains.

It is appropriate to conclude this paper by considering the relative merits of Bessel and Gaussian beams in other laser-driven acceleration mechanisms [35]. This can be accomplished using scaling arguments and assuming that phase synchronism can be maintained by some means. The detailed comparison between analytical calculations and full-scale simulations of the VBWA contained in this paper implies that scaling relationships based on general arguments suffice to within factors of order unity.

The VBWA may be grouped with the laser wakefield accelerator (LWFA) and the plasma beat wave accelerator (PBWA) since they rely on ponderomotive force and the interaction is quadratic in the field strength [5]. The cyclotron autoresonance accelerator (CARA) [50–54], inverse free-electron laser (IFEL) [20], and inverse Čerenkov accel-

TABLE III. Comparison of Bessel and Gaussian laser beams for acceleration.

| Acceleration mechanism | Ratio of accel. length $L^{(B)}/L^{(G)}$ | Ratio of accel. gradient $E^{(B)}/E^{(G)}$ | Ratio of final energy $W^{(B)}/W^{(G)}$ |
|---|---|---|---|
| IFEL | $N(w^{(B)}/w^{(G)})^2$ | $(w^{(G)}/w^{(B)})(P^{(B)}/NP^{(G)})^{1/2}$ | $(w^{(B)}/w^{(G)})(NP^{(B)}/P^{(G)})^{1/2}$ |
| CARA | $N(w^{(B)}/w^{(G)})^2$ | $(w^{(G)}/w^{(B)})(P^{(B)}/NP^{(G)})^{1/2}$ | $(w^{(B)}/w^{(G)})(NP^{(B)}/P^{(G)})^{1/2}$ |
| ICA | $N(w^{(B)}/w^{(G)})^2$ | $(w^{(G)}/w^{(B)})^2(P^{(B)}/NP^{(G)})^{1/2}$ | $(NP^{(B)}/P^{(G)})^{1/2}$ |
| VBWA | $N(w^{(B)}/w^{(G)})^2$ | $(w^{(G)}/w^{(B)})^2(P^{(B)}/NP^{(G)})$ | $P^{(B)}/P^{(G)}$ |
| LWFA | $N(w^{(B)}/w^{(G)})^2$ | $(w^{(G)}/w^{(B)})^2(P^{(B)}/NP^{(G)})$ | $P^{(B)}/P^{(G)}$ |
| PBWA | $N(w^{(B)}/w^{(G)})^2$ | $(w^{(G)}/w^{(B)})^2(P^{(B)}/NP^{(G)})$ | $P^{(B)}/P^{(G)}$ |
| VA | $(w^{(B)}/w^{(G)})^2$ | $(w^{(G)}/w^{(B)})^2(P^{(B)}/NP^{(G)})^{1/2}$ | $(P^{(B)}/NP^{(G)})^{1/2}$ |

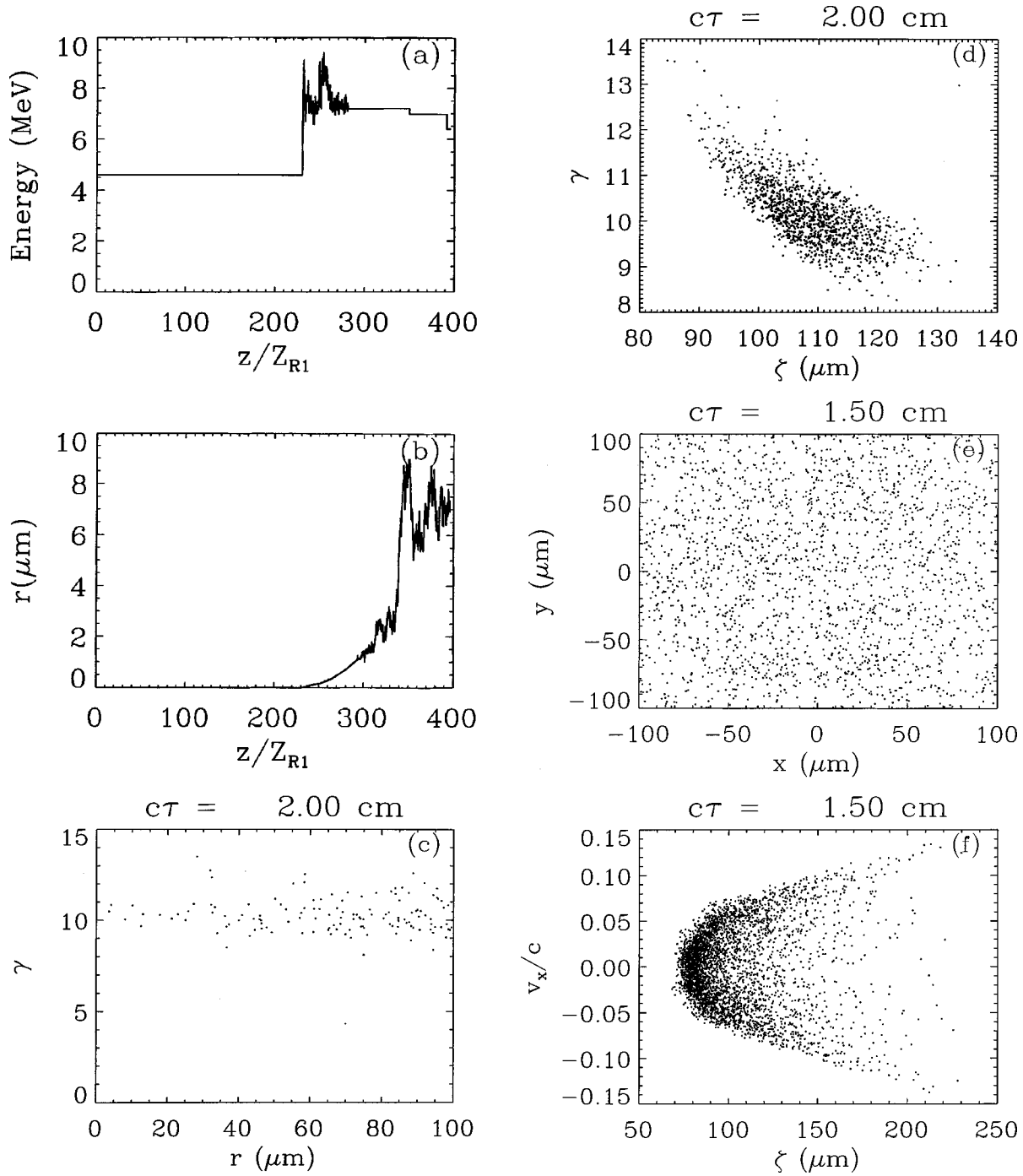


FIG. 10. Simulation results for VBWA driven by Bessel laser beams—formed by a compound axicon optical element—employing initially converging 4.5-MeV finite-emittance particle beam. Particles are injected well upstream of the (common) overlap region of the axicon beams. Plots of (a) peak energy, (b) centroid radius are shown as functions of $z/Z_{R1}$, while (c) and (d) show radial and axial phase-space plots at end of run, $c\tau=2$. The $x$-$y$ and $\zeta$-$v_x/c$ plots, (e) and (f), respectively, are at $c\tau=1.5$.

erator (ICA) [15] mechanisms have in common the property of being linear in the laser-field strength. Finally, the vacuum accelerator (VA) [7,12,15], driven by a single laser beam, is exceptional since the acceleration distance is limited by phase slippage. In all the examples, the change in energy is written as $W=EL$, where $E$ is the acceleration gradient and $L$ is the acceleration distance. The outline of the scaling argument for the ICA is as follows. In the ICA, the change in electron energy is the result of interaction with the axial component of the laser electric field $\varepsilon_z$ and can therefore be written as

$$W\propto\varepsilon_z L. \tag{65}$$

From Eqs. (1)–(3), for a Gaussian beam $\varepsilon_z \propto[P^{(G)}]^{1/2}/[w^{(G)}]^2$, where $P^{(G)}$ is the beam power, $L$ is on the order of a Rayleigh range, $L\approx\pi[w^{(G)}]^2/\lambda$, and $w^{(G)}$ replaces the spot size $w_0$ for notational clarity. Hence,

$$W^{(G)}\propto[P^{(G)}]^{1/2}. \tag{66}$$

On the other hand, for a Bessel beam with $N$ lobes $\varepsilon_z$

$\propto [P^{(B)}/N]^{1/2}/[w^{(B)}]^2$, where $P^{(B)}$ is the *total* beam power, $L = N\pi[w^{(B)}]^2/\lambda$ and $w^{(B)}$ is the radius of the *central* lobe. Hence,

$$W^{(B)} \propto [NP^{(B)}]^{1/2}. \tag{67}$$

Combining Eqs. (66) and (67), it follows that

$$W^{(B)}/W^{(G)} \sim [NP^{(B)}/P^{(G)}]^{1/2}. \tag{68}$$

For equal powers, this ratio scales as $N^{1/2}$. Thus for the ICA, it is advantageous to employ Bessel beams as compared to Gaussian beams, the more so as $N$ increases. Table III compares the Gaussian and Bessel beams for the various mechanisms, listing the ratio of acceleration lengths, acceleration gradients, and final energies. The following remarks should be noted. First, in the high-intensity limit $a_0 \equiv |e|\varepsilon_0/(mc\omega) \gg 1$ the scaling of the LWFA changes to favor the Bessel beam since the wakefield amplitude $\propto a_0^2/(1+a_0^2)^{1/2}$ then becomes proportional to the *first* power of the laser field [5]. Second, for brevity the entries for the VBWA and the PBWA—involving two laser beams—assume that the laser power in each beam is the same. Finally, in the VA the acceleration distance is limited by phase slippage independent of the beam profile.

## ACKNOWLEDGMENTS

The authors are grateful to Professor J. L. Hirshfield for valuable discussions. This work was supported by a DOE Small Business Innovation Research (SBIR) Grant to Omega-P, Inc., and carried out under a Cooperative Research and Development Agreement (CRADA) between the Naval Research Laboratory and Omega-P, Inc. A portion of this work was also supported by the Division of High Energy Physics, Office of Energy Research, U.S. Department of Energy and by the Office of Naval Research.

[1] *Advanced Accelerator Concepts*, edited by P. Schoessow, AIP Conf. Proc. No. 335 (American Institute of Physics, New York, 1995).

[2] *Second Generation Plasma Based Accelerators*, edited by T. Katsouleas and R. Bingham, IEEE Trans. Plasma Sci. PS-24, (1996).

[3] *Advanced Accelerator Concepts*, edited by S. Chattopadhyay, AIP Conf. Proc. No. 398 (American Institute of Physics, New York, 1997).

[4] A. Ting, C. I. Moore, K. Krushelnick, C. Manka, E. Esarey, P. Sprangle, R. Hubbard, H. R. Burris, R. Fischer, and M. Baine, Phys. Plasmas **4**, 1889 (1997); C. I. Moore, A. Ting, K. Krushelnick, E. Esarey, R. F. Hubbard, B. Hafizi, H. R. Burris, C. Manka, and P. Sprangle, Phys. Rev. Lett. **79**, 3909 (1997).

[5] E. Esarey, P. Sprangle, J. Krall, and A. Ting, IEEE Trans. Plasma Sci. **PS-24**, 252 (1996); Phys. Fluids B **5**, 2690 (1993).

[6] P. Sprangle, E. Esarey, and J. Krall, Phys. Plasmas **3**, 2183 (1996); Phys. Rev. E **54**, 4211 (1996).

[7] Y. Liu, D. Cline, and P. He, Nucl. Instrum. Methods Phys. Res. A **424**, 296 (1999).

[8] J. A. Edighoffer and R. H. Pantell, J. Appl. Phys. **50**, 6120 (1979).

[9] E. J. Bochove, G. J. Moore, and M. O. Scully, Phys. Rev. A **46**, 6640 (1992).

[10] U. Mohideen, H. W. K. Tom, R. R. Freeman, J. Bokor, and P. H. Bucksbaum, J. Opt. Soc. Am. B **9**, 2190 (1992).

[11] E. Esarey, P. Sprangle, and J. Krall, Phys. Rev. E **52**, 5443 (1995); P. Sprangle, E. Esarey, J. Krall, and A. Ting, Opt. Commun. **124**, 69 (1996).

[12] Y. C. Huang, D. Zheng, W. M. Tullahard, and R. L. Byer, Appl. Phys. Lett. **68**, 753 (1996); Y. C. Huang and R. L. Byer, *ibid.* **69**, 2175 (1996).

[13] B. Hafizi, A. Ting, E. Esarey, P. Sprangle, and J. Krall, Phys. Rev. E **55**, 5924 (1997).

[14] J. R. Fontana and R. H. Pantell, J. Appl. Phys. **54**, 4285 (1983).

[15] R. D. Romea and W. D. Kimura, Phys. Rev. D **42**, 1807 (1990); S. C. Tidwell, D. H. Ford, and W. D. Kimura, Opt. Eng. (Bellingham) **31**, 1527 (1992); L. C. Steinhauer and W. D. Kimura, J. Appl. Phys. **72**, 3237 (1992); W. D. Kimura, G. H. Kim, R. D. Romea, L. C. Steinhauer, I. V. Pogorelsky, K. P. Kusche, R. C. Fernow, X. Wang, and Y. Liu, Phys. Rev. Lett. **74**, 546 (1995).

[16] T. B. Zhang, T. C. Marshall, M. L. LaPointe, J. L. Hirshfield, and A. Ron, Phys. Rev. E **54**, 1918 (1996).

[17] R. B. Palmer, J. Appl. Phys. **43**, 3014 (1972).

[18] P. Sprangle and C. M. Tang, IEEE Trans. Nucl. Sci. **NS-28**, 3346 (1981).

[19] R. H. Pantell and T. I. Smith, Appl. Phys. Lett. **40**, 753 (1982).

[20] T. C. Marshall, A. Bhattacharjee, S. Y. Cai, Y. P. Chou, and I. Wernick, Nucl. Instrum. Methods Phys. Res. A **304**, 683 (1991); I. Wernick and T. C. Marshall, Phys. Rev. A **46**, 3566 (1992); T. B. Zhang and T. C. Marshall, Phys. Rev. E **50**, 1491 (1994); A. van Steenbergen, J. Gallardo, J. Sandweiss, and J. M. Fang, Phys. Rev. Lett. **77**, 2690 (1996); R. B. Yoder, T. B. Zhang, T. C. Marshall, and J. L. Hirshfield, in Ref. [3], p. 629.

[21] B. Quesnel and P. Mora, Phys. Rev. E **58**, 3719 (1998).

[22] A. E. Siegman, *Lasers* (University Science Books, Mill Valley, CA, 1986).

[23] J. Durnin, J. J. Miceli, and J. H. Eberly, Phys. Rev. Lett. **58**, 1499 (1987); J. Durnin, J. Opt. Soc. Am. A **4**, 651 (1987).

[24] Y. Y. Ananev, Opt. Spektrosk. **64**, 1211 (1988) [Opt. Spectrosc. **64,** 722 (1988)].

[25] J. Turunen, A. Vasara, and A. T. Friberg, Appl. Opt. **27**, 3959 (1988); A. Vasara, J. Turunen, and A. T. Friberg, J. Opt. Soc. Am. A **6**, 1748 (1989).

[26] G. Indebetouw, J. Opt. Soc. Am. A **6**, 150 (1989).

[27] G. Scott and N. McArdle, Opt. Eng. (Bellingham) **31**, 2640 (1992).

[28] P. Sprangle and B. Hafizi, Phys. Rev. Lett. **66**, 837 (1991).

[29] B. Hafizi and P. Sprangle, J. Opt. Soc. Am. A **8**, 705 (1991).

[30] M. R. Lapointe, Opt. Laser Technol. **24**, 315 (1992).

[31] C. Patterson and R. Smith, Opt. Commun. **124**, 121 (1996).

[32] S. C. Tidwell, G. H. Kim, and W. D. Kimura, Appl. Opt. **32**, 5222 (1993).

[33] I. V. Pogorelsky, W. D. Kimura, and Y. Liu, in *Advanced*

*Accelerator Concepts* (Ref. [1]), p. 419.
[34] C. G. Durfee III and H. M. Milchberg, Phys. Rev. Lett. **71**, 2409 (1993); C. G. Durfee III, J. Lynch, and H. M. Milchberg, Phys. Rev. E **51**, 2368 (1995).
[35] B. Hafizi, E. Esarey, and P. Sprangle, Phys. Rev. E **55**, 3539 (1997).
[36] J. W. Goodman, *Introduction to Fourier Optics* (McGraw-Hill, New York, 1988).
[37] J. D. Jackson, *Classical Electrodynamics* (Wiley, New York, 1975).
[38] P. W. Milonni and J. H. Eberly, *Lasers* (Wiley, New York, 1988).
[39] S. Ramo, J. R. Whinnery, and T. van Duzer, *Fields and Waves in Communication Electronics* (Wiley, New York, 1984), Chap. 14.
[40] B. Hafizi, J. Appl. Phys. **73**, 513 (1993).
[41] E. Hecht, *Optics* (Addison-Wesley, Reading, MA, 1998).
[42] O. Carnal, M. Sigel, T. Sleator, H. Takuma, and J. Mlynek, Phys. Rev. Lett. **67**, 3231 (1991).
[43] N. M. Ceglio, J. X-Ray Sci. Technol. **1**, 7 (1989).
[44] J. H. McLeod, J. Opt. Soc. Am. **44**, 592 (1954).
[45] V. V. Korobkin, L. Ya. Polonskii, V. P. Poponin, and L. N. Pyatnitskii, Kvant. Elektron. (Moscow) **13**, 265 (1986) [Sov. J. Quantum Electron. **16,** 178 (1986)].
[46] O. G. Ivanov, R. I. Okunev, L. N. Pakhomov, V. Yu. Petrun'kin, L. Ya. Polonskii, and L. N. Pyatnitskii, Zh. Tekh. Fiz. **57**, 2012 (1987) [Sov. Phys. Tech. Phys. **32,** 1212 (1987)].
[47] R. Tremblay, Y. D'Astous, G. Roy, and M. Blanchard, Opt. Commun. **28**, 193 (1979).
[48] D. Gordon, C. E. Clayton, T. Katsouleas, W. B. Mori, and C. Joshi, Phys. Rev. E **57**, 1035 (1998).
[49] C. K. Birdsall and A. B. Langdon, *Plasma Physics via Computer Simulation* (McGraw-Hill, New York, 1985).
[50] P. Sprangle, L. Vlahos, and C. M. Tang, IEEE Trans. Nucl. Sci. **NS-30**, 3177 (1983).
[51] C. Chen, Phys. Fluids B **3**, 2933 (1991); Phys. Rev. A **46**, 6654 (1992).
[52] B. Hafizi, P. Sprangle, and J. L. Hirshfield, Phys. Rev. E **50**, 3077 (1994).
[53] C. Wang and J. L. Hirshfield, Phys. Rev. E **51**, 2456 (1995).
[54] M. A. LaPointe, R. B. Yoder, C. Wang, A. K. Ganguly, and J. L. Hirshfield, Phys. Rev. Lett. **76**, 2718 (1996).